



Published in final edited form as:

*Abdom Radiol (NY)*. 2021 July ; 46(7): 3288–3300. doi:10.1007/s00261-021-02984-2.

## Ferumoxylol Enhanced Ultrashort TE MRA and Quantitative Morphometry of the Human Kidney Vasculature

Liam Timms<sup>1,9</sup>, Tianyi Zhou<sup>1,9</sup>, Yue Lyu<sup>1</sup>, Ju Qiao<sup>2</sup>, Vishala Mishra<sup>3</sup>, Rita Maria Lahoud<sup>3</sup>, Gayatri Veeramani Jayaraman<sup>4,5</sup>, Andrew S. Allegretti<sup>4</sup>, David Drew<sup>6</sup>, Ravi T. Seethamraju<sup>7</sup>, Mukesh Harisinghani<sup>3</sup>, Srinivas Sridhar<sup>1,8</sup>

<sup>1</sup>Northeastern University, Boston, MA, United States

<sup>2</sup>Massachusetts General Hospital, Boston, MA, United States

<sup>3</sup>Radiology, Massachusetts General Hospital, Boston, MA, United States

<sup>4</sup>Nephrology, Massachusetts General Hospital, Boston, MA, United States

<sup>5</sup>Nephrology, Brigham and Women's Hospital, Boston, MA, United States

<sup>6</sup>Tufts Medical Center, Boston, MA, United States

<sup>7</sup>Siemens Medical Solutions, Boston, MA, United States

<sup>8</sup>Theranano LLC, Newton, MA, United States

<sup>9</sup>These authors share first authorship

### Abstract

**Purpose:** To evaluate the feasibility of Quantitative Ultrashort-Time-to-Echo Contrast Enhanced (QUTE-CE) MRA using ferumoxylol as a contrast agent for abdominal angiography in the kidney.

**Correspondence:** Srinivas Sridhar, 435 Egan Research Center, 120 Forsyth Street, Boston, MA 02115. Tel: 617-373-2930. Fax: 617-373-2823. s.sridhar@northeastern.edu.

**Authors' contributions:** LT, MH and SS contributed to the study concept and design. LT, JQ, RML, VM, AA, GVJ and MH contributed to data acquisition. Data analysis was performed by LT, TZ and YL. The manuscript was drafted by LT, TZ and SS. Critical editing and revision of the manuscript was done by LT, TZ, SS, RTS, and DD. All authors read and approved the final manuscript.

**Publisher's Disclaimer:** This Author Accepted Manuscript is a PDF file of an unedited peer-reviewed manuscript that has been accepted for publication but has not been copyedited or corrected. The official version of record that is published in the journal is kept up to date and so may therefore differ from this version.

Declarations

**Conflicts of interest:** RTS reports personal fees from Siemens Medical Solutions, Inc., outside the submitted work. SS reports grants from Theranano LLC and grants from Northeastern University, during the conduct of the study; In addition, SS has a patent WO2017019182A1 pending.

**Ethics approval:** This study was conducted with approval by the Massachusetts General Hospital Institutional Review board IRB:2017P001262. All procedures performed in the study involving human participants were Health Insurance Portability and Accountability Act (HIPAA) compliant.

**Consent to participate:** Subjects provided informed written consent for the imaging procedure which is an off-label use of ferumoxylol.

**Consent for publication:** Not applicable.

**Availability of data and material:** All data analyzed during this study were included in this manuscript and its supplementary information.

**Code availability:** Advanced Normalization Toolkit (ANTS, <http://stnava.github.io/ANTS/>), 3D Slicer (<http://www.slicer.org>), Vascular Modeling ToolKit (VMTK, [www.vmtk.org](http://www.vmtk.org))

**Methods:** Four subjects underwent ferumoxytol-enhanced MRA with the 3D UTE Spiral VIBE WIP sequence at 3T. Image quality metrics were quantified, specifically the blood Signal-to-Noise Ratio (SNR), blood-tissue Contrast-to-Noise Ratio (CNR) and Intraluminal Signal Heterogeneity (ISH) from both the aorta and inferior vena cava (IVC). Morphometric analysis of the vessels was performed using manual approach and semi-automatic approach using Vascular Modeling ToolKit (VMTK). Image quality and branching order were compared between QUTE-CE MRA and the Gadolinium (Gd) CEMRA reference image.

**Results:** QUTE-CE MRA provides a bright blood snapshot that delineates arteries and veins equally in the same scan. The maximum SNR and CNR values were  $3,282 \pm 1,218$  and  $1,295 \pm 580$ , respectively – significantly higher than available literature values using other CEMRA techniques. QUTE-CE MRA had lower ISH and depicted higher vessel branching order (7<sup>th</sup> vs 3<sup>rd</sup>) within the kidney compared to a standard dynamic clinical Gd CEMRA scan. Morphometric analysis yielded quantitative results for the total kidney volume, total cyst volume and for diameters of the branching arterial network down to the 7<sup>th</sup> branch. Vessel curvature was significantly increased ( $p < 0.001$ ) in the presence of a renal cyst compared to equivalent vessels in normal kidney regions.

**Conclusion:** QUTE-CE MRA is feasible for kidney angiography, providing greater detail of kidney vasculature, enabling quantitative morphometric analysis of the abdominal and intrarenal vessels and yielding metrics relevant to vascular diseases while using a contrast agent ferumoxytol that is safe for CKD patients.

## Keywords

Ultrashort Time-to-Echo; Ferumoxytol; Chronic Kidney Disease; MRA; Vascular

## Introduction

Approximately 1 in 7 US adults suffer from chronic kidney disease (CKD) [1], a progressive disease with a high burden of comorbidity and an association with vascular pathologies related to declining kidney function. Currently, blood biomarkers (e.g. serum creatinine) are used to diagnose CKD. Yet, they can only reflect the overall performance of the kidney at the time of the blood-draw and do not provide reliable etiologic or prognostic evaluation of kidney pathology [2, 3]. In contrast, imaging biomarkers offer the potential to monitor the pathological progression of the disease and thus hold promise for diagnosing not only the presence but also etiology of kidney disease [3, 4].

Contrast Enhanced Magnetic Resonance Angiography (CEMRA) with gadolinium (Gd) based contrast agents (GBCAs) provides excellent sensitivity and high-resolution imaging of the vasculature. It is well accepted as a reliable method for detecting renal artery stenosis [5]. However, Gd CEMRA must be used with caution in patients with CKD due to the risks of nephrogenic systemic fibrosis (NSF) caused by the nephrotoxicity of free Gd ions dissociated from the chelate [6]. Despite the development of alternative GBCAs to alleviate these risks, most nephrology guidelines continue to recommend avoidance of GBCAs whenever possible in CKD patients [7–9].

Unfortunately, other imaging techniques have not been able to meet this critical need of a safe imaging modality for CKD patients. Computed Tomography (CT) imaging with contrast can provide kidney vascular images; however, CT involves radiation exposure and the administration of iodinated contrast which carries an even higher risk of acute kidney injury [10, 11]. Renal ultrasounds avoid the use of nephrotoxic contrast media but limitations in image quality and sensitivity preclude the ability to identify CKD etiology and severity [10]. Non-contrast-enhanced MRA techniques are occasionally used in this population but their clinical use is limited by the dependence on flow directionality, and sensitivity to off-resonance effects [12]. Therefore, CEMRA remains the most promising modality for angiography of CKD patients and the development of non-Gd-based CEMRA alternatives is a major unmet need of significant clinical relevance.

The potential of the super-paramagnetic iron oxide nanoparticle (SPION) contrast agent ferumoxytol as an alternative to GBCA in CKD patients has been widely recognized [13–15]. Unlike GBCAs which washed out from blood pool rapidly and cleared through renal filtration, ferumoxytol acts as a stable blood-pool contrast agent with a long half-life of 14–21 hours [16] and remains intravascular, even in the kidney, during this period. Instead of renal secretion, it is taken up by mononuclear phagocyte system cells, after which the iron is incorporated into the body's iron stores [17]. This extends the imaging time window and allows vessel enhancement of both arteries and veins to the same extent in a single scan. Furthermore while observations of Gd deposition in the brain have raised concern [18], a recent study did not find iron deposition in the brain of pigs with ferumoxytol as MRI contrast agent [19]. Long-term studies of the human brain after iron oxide administration have not been reported so far.

Since iron has strong susceptibility effects, T2\* weighted negative contrast was a natural approach to SPION imaging, however negative contrast is unappealing to radiologists as signal voids are difficult to evaluate visually [17]. Positive contrast imaging with ferumoxytol using routine T1 weighted sequences has been explored, yet susceptibility artifacts reduce image quality [16]. Other positive contrast techniques like IRON [20] have been proposed but suffer from additional artifacts. The continued development of Ultra-short-Time-to-Echo (UTE) sequences has enabled a new way to generate positive contrast with SPIONs with some significant advantages. In 2017, Gharagouzloo et al. [21] demonstrated the Quantitative Ultra-short-Time-to-Echo Contrast Enhanced (QUTE-CE) MRA protocol with ferumoxytol in animal models and showed advantages to angiographic quality and quantitative measurements. In 2019, Knobloch et al. [22] demonstrated the use of another UTE protocol with ferumoxytol for pulmonary CEMRA in humans.

Here for the first time in humans, we translated the QUTE-CE MRA technique to a clinical scanner and evaluated the potential of the technique for kidney imaging, in subjects with normal kidneys and a CKD patient. The goal of this study is to demonstrate the feasibility of the QUTE-CE MRA technique for human kidney imaging by providing angiographic and morphologic metrics of the kidney vasculature.

## Materials and Methods

### Study Volunteers

This prospective feasibility study was conducted with approval of Mass General Brigham Institutional Review board. All procedures were completed between July to August of 2018 and were Health Insurance Portability and Accountability Act (HIPAA) compliant. Subjects (1M 3F) were recruited from a pool of patients independently prescribed for 510 mg ferumoxytol infusion (Feraheme; AMAG Pharmaceuticals, Waltham, MA) as part of their regular standard of care as an iron supplement. Subject information is provided in Table 1. One subject had stage 5 CKD (eGFR = 10 mL/min/1.73m<sup>2</sup>). The others did not have known kidney dysfunction. Ferumoxytol infusion and monitoring were completed by the Massachusetts General Hospital independent of this imaging study. Subjects provided written informed consent for the imaging procedure. The abdominal images reported here were captured from a subset of subjects (4 subjects) enrolled in a larger neuroimaging study (15 subjects), using additional scan time when available.

For the purpose of comparison analysis, we obtained the clinical Gd CEMRA data of one patient from our collaborators at Massachusetts General Hospital. The Gd CEMRA acquisition was not part of this study and it was performed in November 2019 with 20 ml of Dotarem (Guerbet, Paris, France). The data was de-identified and analyzed retrospectively.

### Imaging Protocol

Imaging was conducted at the Athinoula A. Martinos Center for Biomedical Imaging (Boston, MA) using a 3T scanner (MAGNETOM Prisma, Siemens Healthcare, Erlangen, Germany). The scan protocol consisted of a single post-contrast session lasting ~20 minutes completed 45 minutes to 2 hours after ferumoxytol infusion. Siemens Spine Matrix 32 coils and Body 18 Coils were used as receive coils. Spine coil elements were selected to suit each subject's body size and positioning while all body coil elements were kept active.

UTE scans were acquired with a prototype 3D spiral UTE VIBE sequence (Siemens Works In Progress UTE Spiral VIBE). This sequence consists of a non-slice-selective 3D excitation with a stack of spirals trajectory during readout. The TE minimization option was enabled, providing the minimum TE of 0.05 ms on all QUTE-CE scans. The QUTE-CE scans were acquired in 2 types; 1) *breath-hold scans* lasting 16 seconds, 2) a *free-breathing scan* using Gating Control. The Gating Control signal is obtained from an element of the spine coil selected via the sequence user interface. In this mode, the frequency data is acquired normally as long as the gating condition is satisfied and reacquired only if it does not satisfy the condition. The average acquisition time lasts approximately 12 minutes but is variable based on subject breathing patterns. Within the breath-hold regime, two different parameter sets were tested. The sequence parameters are reported in Table 1. The per-subject variations in imaging protocol were due to per-subject variation in SAR limits and abdominal dimensions.

The Gd CEMRA reference images used for comparison were obtained retrospectively and were acquired on another Siemens 3T PRISMA scanner as part of existing clinical

procedures at Massachusetts General Hospital using a standard T1-weighted VIBE sequence. The sequence parameters are reported in Table 1.

### Image Analysis and Segmentation

All images were pre-processed with the N4ITK bias field correction [23] implemented in the Advanced Normalization Toolkit (ANTs) [24]. The correction was calculated and applied within a mask covering the majority of abdomen in the FOV but excluding the surrounding air. All relevant regions of interest (ROIs) were segmented and cropped from the corrected images using 3D Slicer (<http://www.slicer.org>) [25].

**Angiographic analysis.**—Signal-to-Noise Ratio (SNR) was quantified by extracting the mean signal intensity of an ROI in the inferior vena cava (IVC) and abdominal aorta, and dividing it by the standard deviation of the noise measured in an ROI in the air outside the body. The ROI of IVC and abdominal aorta was manually selected using 3DSlicer from an automatically generated vesselness probability map. The vesselness probability map was calculated with the vesselness filtering function in the Vascular Modeling ToolKit (VMTK, [www.vmtk.org](http://www.vmtk.org)) and the manual ROI was restricted to voxels with vesselness probability above 97% forming a contiguous selection within the lumen of these large vessels. The ROI for the noise calculation was chosen to avoid motion artifacts near the surface of the body if present. Intraluminal Signal Heterogeneity (ISH) was previously defined in Sigovan et al. [26] to assess the homogeneity of luminal signal enhancement. It was defined as the ratio of the standard deviation to the mean signal intensity in the same luminal ROI. The Contrast-to-Noise Ratio (CNR) was defined as the difference from the blood SNR to the tissue SNR. The tissue mean signal intensity was measured from an ROI in the right suprarenal gland, avoiding any visible blood vessels. The blood SNR, ISH and blood-tissue CNR were the average of those in IVC and abdominal aorta for QUTE-CE MRA scans while just abdominal aorta for Gd CEMRA reference scans. The angiographic analysis processing pipeline took about 3 min per subject.

**Morphometric analysis.**—Morphometric analysis of the vessels was performed using two approaches – a manual approach done in 3D Slicer and a semi-automatic approach using VMTK. The manual measurement of vessel diameters was made as follows: (a) the inferior vena cava (IVC) and the abdominal aorta were segmented manually from the free-breathing images. (b) 3 evenly spaced-out points along the IVC and aorta were chosen as measurement locations. (c) At each location of measurement, one author measured both the anteroposterior (AP) and transverse (T) diameters across the IVC and aorta. In the aorta both AP and T may be considered diameter measurements due to the circular cross-section [27].

The semi-automatic approach is described as follows: (a) IVC, aorta, renal arteries and intra-renal vessels were segmented manually from breath-hold and free-breathing images. (b) Surface models of the vessel walls were generated with VMTK's marching cubes algorithm. (c) Start and end points were defined for individual vessel segments of interest. (d) Using VMTK's Voronoi-diagram-based approach for automated centerline computation, 35 to 221 centerline points were calculated for each vessel segment. The centerline calculation

provided the spatial coordinates and the distance from the centerline to the vessel surface model at each point. The following parameters were then extracted:

1. Branching order of each segment was defined as the number of bifurcations traversed from the root branch to that segment. The branches were labeled from the root branch out to the terminal branch of the vessel. We chose the abdominal aorta as the root branch (1<sup>st</sup> order) in all scans.
2. Vessel diameter was defined as two times minimum Euclidian distance from surface points to a centerline. Diameter of the renal artery was measured by taking the mean and standard deviation of diameters at these centerline points in renal artery segment. The computed centerline of renal artery consists of 35 – 65 centerline points. The degree of narrowing was defined as the difference between mean diameter and minimum diameter of the vessel as a percentage of the mean diameter of the vessel.
3. Vessel curvature was defined as the reciprocal of the radius of the osculating circle at each centerline point. This metric was specifically quantified in the vessels surrounding a cyst by segmenting vessels with an ROI at the 3<sup>rd</sup> branching order. This was done in the kidney bearing the largest cyst present in our subjects and in the corresponding vessels at 3<sup>rd</sup> branching order in the other non-cyst bearing kidney of the same subject. Curvature was compared between 132 and 102 centerline points in vessels in the cyst-bearing area of the left kidney and in the corresponding area on the non-cyst-bearing right kidney by Welch's t test. The significance threshold was set to  $P < 0.05$ . Statistical analysis was performed using Python's SciPy library (1.3.1).

Finally, the borders of each whole kidney and any present cysts were manually cropped from the images and volumes of kidney and cysts were calculated via the quantification module of 3D Slicer.

## Results

### Angiographic analysis

Positive contrast CEMRA images of the human abdomen were acquired via application of the QUTE-CE MRA technique. These images captured all central and peripheral vessels (both arterial and venous) within the field of view in the abdominal cavity down to the limits of the resolution (Figure 1). The field-of-view of covered multiple abdominal organs but was positioned to capture both kidneys which could then be cropped from the full image (Figure 1). Renderings for breath-hold and free-breathing QUTE-CE MRA are provided in Supplemental Figure S1.

Quantitative metrics of angiographic quality were assessed for breath-hold QUTE-CE, free-breathing QUTE-CE and Gd CEMRA (Table 1). First, QUTE-CE produced similar enhancement of arteries and veins. By averaging the artery and vein metrics, the maximum SNR and CNR values were  $3,282 \pm 1,218$  and  $1,295 \pm 580$  for breath-hold QUTE-CE,  $181 \pm 59$  and  $111 \pm 64$  for free-breathing QUTE-CE, respectively. Second, free-breathing QUTE-CE gives comparable SNR ( $182 \pm 64$  vs  $134$  for artery,  $181 \pm 70$  vs  $106$  for vein),



comparable CNR ( $111 \pm 29$  vs 97 for artery,  $111 \pm 35$  vs 69 for vein), and lower ISH ( $0.068 \pm 0.022$  vs  $0.228$  for artery,  $0.058 \pm 0.011$  vs  $0.081$  for vein) at a higher resolution ( $4.05 \pm 0.35 \text{ mm}^3$  vs  $5.56 \text{ mm}^3$ ) compared to Gd CEMRA delayed phase 2.

## Morphometric analysis and Segmentations

**Branching order.**—QUTE-CE MRA displayed vessel branching up to the 7th order while the Gd CEMRA reference image displayed vessel branching only to 3rd order (Figure 2). This was the case in both the dynamic first pass image and the subsequent delayed phase Gd CEMRA images.

**Vessel diameter.**—Using manual approach, anteroposterior (AP) and transverse (T) diameters were measured in the IVC and aorta. As shown in Figure 3, IVC has an elliptical cross-section and transverse diameters were about twice AP diameter ( $22.1 \pm 2.6 \text{ mm}$  vs  $12.3 \pm 1.1 \text{ mm}$ ). While for the aorta, cross-section was circular with transverse and AP diameters within standard deviation ( $17.6 \pm 4.6 \text{ mm}$  vs  $16.5 \pm 4.0 \text{ mm}$ ). Due to this morphological difference, veins must be assessed along two axes but only one axis is necessary for artery diameter extraction.

Using the VMTK semi-automatic approach, vessel diameters were extracted from the arteries (aorta, renal artery, intra-renal arteries, Figure 4a,b) and veins (IVC, renal vein, intra-renal veins, Figure 4c,d). The aorta diameter measurements were within standard deviation between the manual approach ( $17.1 \pm 4.3 \text{ mm}$ ) and the semi-automatic approach ( $16.3 \pm 3.8 \text{ mm}$ ). This approach was then applied to the arterial network extending from the aorta into the kidney itself (Figure 4). The average renal artery diameter (with standard deviation of the automatic points along the artery) from this method are provided in Table 2. In one subject, a narrowing of the left renal artery could be visually identified (Figure 5a) and was quantified as a 28.7% reduction (4.8 mm at the narrowest measured centerline point compared to the average renal artery diameter 6.8 mm for the rest of the segment). This narrowing was not observed in the corresponding right renal artery of the same subject (Figure 5c).

**Vessel curvature.**—One subject presented with a large cyst on the left kidney but not the right kidney. Vascular disruption in the area of the cyst could be visually observed (Figure 6). Vessel curvature was extracted for regions of 3rd branching order in the corresponding areas of both kidneys. In the region of the large cyst, the mean curvature was  $0.06 \pm 0.04$  compared to  $0.05 \pm 0.03$  in the other kidney. There was a statistically significant ( $P < 0.001$ ) difference between the values for the right and the left kidney (Figure 6).

**Kidney and cyst volumes.**—From the QUTE-CE MRA images, total kidney volumes, cyst volumes and the cyst/kidney ratio were calculated (Table 2). The Pearson correlation coefficient,  $r$ , was calculated for each combination of physical attributes presented in Table 2. The highest magnitude correlation was kidney volume with renal artery diameter ( $r = 0.80$ ). The next highest magnitude  $r$ -values were correlations with age: average renal artery diameter with subject age ( $r = -0.70$ ), the kidney volume with subject age ( $r = -0.69$ ).

## Discussion

This study demonstrated the translation of QUTE-CE MRA to abdominal (specifically kidney) angiography for the first time in humans. QUTE-CE MRA provided a bright blood high contrast image of arteries and veins equally in the same scan. Arteries, veins, kidneys and cysts were identified and segmented from the image. Differences between artery and vein morphology were observed and measurements of the kidney vasculature were extracted in new detail up to the 7<sup>th</sup> branching order. We utilized standard clinical Gd CEMRA abdominal scan of a subject taken at the same institution as a comparator retrospectively. QUTE-CE MRA is a potentially useful technique for kidney angiography, providing details of kidney vasculature, enabling quantitative morphometric analysis of the abdominal and intrarenal vessels and yielding clinically relevant metrics while using a blood pool contrast agent, ferumoxytol, that is safe for CKD patients.

The qualitative visual quality of QUTE-CE MRA is reflected quantitatively as very high SNR and CNR values. Surveying recent literature, the average maximum reported SNR of Gd CEMRA at 3T is approximately 102 [29–35] which is lower than all values reported here. The measured SNR for QUTE-CE MRA breath-hold scans is up to 16 times higher compared to the sample data we obtained for an exemplary clinical breath-hold Gd CEMRA. Even at higher spatial resolution (and with a larger field-of-view), CNR for QUTE-CE MRA free-breathing scans remains comparable to the clinical breath-hold Gd CEMRA ( $111 \pm 29$  vs  $97$  for artery,  $111 \pm 35$  vs  $69$  for vein). Additionally, ISH was 3–6 times less for QUTE-CE MRA than this Gd CEMRA. This comparison between the clinical Gd CEMRA scan and the QUTE-CE MRA scans is not an indictment of all possible Gd CEMRA approaches, but rather provided as a point of reference between the novel images captured in this study and the current standard of care.

The low ISH measured here is in line with results in a previous study which demonstrated ferumoxytol-enhanced MRA may provide more homogeneous intra-luminal signal enhancement relative to Gd CEMRA in a controlled comparison using traditional sequences [26]. The ISH measured here is 5–10 times lower than the ISH reported for traditional TE ferumoxytol-enhanced MRA used in that study [26]. This lower heterogeneity is attributable to the minimization of flow and susceptibility effects in the QUTE-CE MRA technique, which provides signal enhancement governed by the SPGR equation [28]. By exciting with a 3D non-slice-selective RF pulse combined with a short TR, both blood and tissue in the center of the FOV are brought to their steady-state magnetization during imaging. This eliminates time-of-flight effects of fresh blood flow into the region of interest. By sampling the free induction decay signal at UTE, the strong negative contrast T2\* effects of ferumoxytol are minimized as much as physically possible [36].

Further, relative to the standard clinical Gd CEMRA using an extracellular CA, the QUTE-CE MRA data had superior delineation of higher order vessels within the kidney. This additional vascular detail is primarily attributable to the pharmacokinetic properties of the CA and is present in other T1-weighted techniques using ferumoxytol [14, 37]. Ferumoxytol is cleared through the liver and not the kidney, while standard extracellular fluid (ECF) agents are excreted from the kidney by glomerular filtration and tubular secretion [18]. This



leads to extravascular contrast enhancement in the renal cortex which drastically reduces blood-tissue contrast within the kidney when using ECF agents [38]. Therefore, by taking advantage of the blood-pool kinetics of ferumoxytol, the QUTE-CE MRA technique provides strong signal enhancement in intra-renal vessels for patients regardless of renal pathological state. Note however that imaging during the blood-pool circulation phase results in full venous contamination, i.e. equal signal enhancement of veins and arteries (Table 1). Manual segmentations by two authors separated renal arteries and veins down to the voxel size (Figures 2–6). Contrast enhancement from even higher order vessels was present in the raw images (Figure 1) but could not be effectively differentiated due to the proximity of arterial and venous vessels.

The segmented images produced by this technique enabled both assessment of the renal arteries, as in clinical CEMRA exams, and the addition of novel analysis of vascular disruption within the kidney. In the large vessels, our findings were very consistent with literature: the aortic diameter decreased inferiorly while the IVC was flattened with significantly different anteroposterior and transverse axes, both known aspects of these vessels [27, 39]. Further, examination for renal artery stenosis is a standard clinical procedure and the renal artery diameters ( $5.9 \pm 1.2$  mm) measured here were very consistent with the literature values of  $6.7 \pm 1.9$  mm [40] and  $5.1 \pm 0.9$  mm [41]. Of clinical relevance, a 28.7% stenosis of the proximal renal artery was observed using QUTE-CE MRA. The technique would therefore enable assessment of renal artery stenosis and IVC flattening with a single scan. With the deeper view of kidney vasculature, the QUTE-CE MRA technique provides new potential for identification of distal renal artery stenosis, which is also of significant interest [42]. However, distal renal artery stenosis was not detected in any of the subjects recruited for this feasibility study.

Further, by leveraging the normally inaccessible intra-renal vessels captured by this technique, the vessel curvature of higher order branches within the kidney was quantified for the first time. In a renal-cyst bearing subject, there was a significant increase in the curvature of the intra-renal vessels surrounding the cyst relative to the equivalent vessels (in branching order and position to the renal artery) on the opposite kidney of the same subject (Figure 6). While standard Gd CEMRA does not provide measurements of intra-renal vascular structure, ex-vivo examinations of nephrectomized kidneys have shown disruptions to vascular structure in the presence of cysts [43]. It is therefore conceivable that the quantification of intra-kidney vascular morphology, exemplified by the significant curvature difference measured here, may provide the basis for completely novel biomarkers of kidney disease and disease progression. However, such potential biomarkers will require extensive further study for development and validation beyond this initial demonstration of feasibility.

The potential for ferumoxytol CEMRA had previously been identified in several studies including children [44] and CKD patients [15]. However, most previous work used traditional T1-weighted or T2\*-weighted sequences. So far, there are only few feasibility studies using UTE sequences with ferumoxytol in humans. In 2019, Knobloch et al. [22] demonstrated the use of a UTE sequence with ferumoxytol for pulmonary CEMRA in humans and reported superior image quality relative to both Gd CEMRA and traditional TE ferumoxytol CEMRA in the same subject. This is consistent with the results reported here

although the examined anatomical regions and associated challenges differ. As noted, longer TEs result in greater T2\* loss of the free induction decay signal. With traditional TEs, ferumoxytol contrast intensity is contaminated by a complex dependence on a combination of both imaging and physiological parameters which confounds clinical interpretation and drastically limits clinical/diagnostic use. These effects are minimized in the QUTE-CE MRA technique by use of ultra-short TE where the FID signal acquisition is as near to excitation as possible, limiting spin dephasing and resulting in more homogenous positive contrast throughout the vasculature as a function of concentration.

A variety of scan protocols were tested as potential candidates for further research. Across the tested parameters, the free-breathing scan protocol provided higher resolution images with good image quality suitable for morphological analysis. As the QUTE-CE MRA technique utilizes 3D excitation pulses to repress tissue signal, a large FOV is required to avoid wrap-around artifacts. In breath-hold protocols, scan-times of ~15s are necessary and resolution was reduced to capture the large FOV within the short scan time. Only the renal artery could be assessed in the breath-hold scans as the intra-renal vessels could not be differentiated at the lower resolutions (Supplemental Figure S1). However, the extremely high SNR values may enable higher resolution and accelerated imaging [45], which are SNR-limited in standard techniques.

In the metrics assessed here, a few correlations were observed. Of interest, the kidney volume and renal artery diameters had a linear correlation which fits with the known relationship between kidney health and blood delivery. Notably, the CKD diagnosed subject scored very low relative to the other subjects on both of these metrics (Table 2). The kidney volume and diameter measurements also correlated negatively with age, with the CKD subject also qualifying as the oldest subject enrolled in this study. These results align with known renal pathology [46], supporting the validity of our approach, yet the low subject number precludes significant conclusions from these data.

There were important limitations in this study. First, the sample population is relatively small; allowing only an initial evaluation of the feasibility of the technique for human imaging. Second, our data set is very heterogeneous with a variety of scan parameters investigated across the small number of subjects. Third, motion artifacts persist in the free breathing scans even with the application of gating methods for motion correction. With blood-pool contrast agents, scans may be repeated to compensate for transient issues (e.g. motion) without significant loss of contrast. However, as this feasibility study was confined to utilizing excess scan time in the course of a larger study, we did not have the capacity to repeat scans. While these limitations are vitally important when evaluating the results, we believe they predominantly reflect external constraints on the experimental design rather than fundamental challenges to the underlying approach. The data from this study demonstrate greater potential for applications of QUTE-CE MRA in vascular imaging of the human kidney. Future studies must focus on enrolling larger groups of subjects, examining kidney pathologies, implementing more robust motion correction/compensation schemes, higher resolution imaging, acquisition acceleration, integrations with clinical workflows and further development of novel biomarkers.

QUTE-CE MRA differs from other angiographic techniques due to several significant factors. The long circulating time of the CA ferumoxylol results in uniform population of all vessels: arteries, veins and capillaries. For this reason, all vascular structures appear equally bright, with intensity directly related to the CA concentration in the blood pool. This is also observed in other T1 weighted imaging [14, 37], although susceptibility effects can lead to distortion and signal loss with traditional TE. The minimization of flow and susceptibility effects leads to purely luminal imaging with superior delineation of the vascular structures. Separate scans for arterial and venous imaging are not required as is the case with time-of-flight angiography. While some may perceive the simultaneous visualization of arteries and veins as a drawback, they can be segmented visually or in post-processing. For all these reasons QUTE-CE MRA presents a qualitatively different clinical experience for the radiologist compared with other angiographic techniques.

In summary, we have translated QUTE-CE MRA to clinical abdominal imaging for the first time in humans with high image quality metrics. This method leads to a deep view of the kidney vasculature, yielding precise delineation of vessel sizes, kidney & cyst volumes and potential quantification of vascular abnormalities. These results lay the groundwork for further studies which could lead to insights on kidney disease. Since CKD is accompanied by both progressive vascular disease and kidney fibrosis which needs further understanding, this technique could aid in both basic research and clinical nephrology. The vascular morphometric analysis enabled by the technique may provide the basis for novel biomarkers for characterization of CKD etiologies or detection of patterns of vascular abnormality more generally.

## Supplementary Material

Refer to Web version on PubMed Central for supplementary material.

## Acknowledgments:

We acknowledge Dr. John E. Kirsch for helpful advice on experimental setup.

**Funding:** This study was funded by National Institutes of Health (Grant numbers 1R41DA043974-01 and 1R21DK118449-01).

## References

1. Murphy D, et al., Trends in Prevalence of Chronic Kidney Disease in the United States. *Ann Intern Med*, 2016. 165(7): p. 473–481. [PubMed: 27479614]
2. Waikar SS, et al., Biological Variability of Estimated GFR and Albuminuria in CKD. *Am J Kidney Dis*, 2018. 72(4): p. 538–546. [PubMed: 30031564]
3. Selby NM, et al., Magnetic resonance imaging biomarkers for chronic kidney disease: a position paper from the European Cooperation in Science and Technology Action PARENCHIMA. *Nephrol Dial Transplant*, 2018. 33(suppl\_2): p. ii4–ii14. [PubMed: 30137584]
4. Bellasi A and Raggi P, Vascular imaging in chronic kidney disease. *Curr Opin Nephrol Hypertens*, 2012. 21(4): p. 382–8. [PubMed: 22531162]
5. Josephs SC, Accuracy of Computed Tomographic Angiography and Magnetic Resonance Angiography for Diagnosing Renal Artery Stenosis. *Perspectives in Vascular Surgery and Endovascular Therapy*, 2005. 17(2): p. 180–182. [PubMed: 16110398]

6. Perazella MA, Advanced kidney disease, gadolinium and nephrogenic systemic fibrosis: the perfect storm. *Curr Opin Nephrol Hypertens*, 2009. 18(6): p. 519–25. [PubMed: 19623065]
7. Schieda N, et al., Gadolinium-Based Contrast Agents in Kidney Disease: Comprehensive Review and Clinical Practice Guideline Issued by the Canadian Association of Radiologists. *Can Assoc Radiol J*, 2018. 69(2): p. 136–150. [PubMed: 29706252]
8. Fotenos A Update on FDA approach to safety issue of gadolinium retention after administration of gadolinium-based contrast agents 2018; Available from: <https://www.fda.gov/media/116492/download>.
9. Mahan Mathur MW, MD. Patient evaluation before gadolinium contrast administration for magnetic resonance imaging 2020; Available from: <https://www.uptodate.com/contents/patient-evaluation-before-gadolinium-contrast-administration-for-magnetic-resonance-imaging#H1951507250>.
10. Bongartz G, Mayr M, and Bilecen D, Magnetic resonance angiography (MRA) in renally impaired patients: when and how. *Eur J Radiol*, 2008. 66(2): p. 213–9. [PubMed: 18329834]
11. Mukundan S, et al., Ferumoxytol-Enhanced Magnetic Resonance Imaging in Late-Stage CKD. *Am J Kidney Dis*, 2016. 67(6): p. 984–8. [PubMed: 26786296]
12. Edelman RR and Koktzoglou I, Noncontrast MR angiography: An update. *J Magn Reson Imaging*, 2019. 49(2): p. 355–373. [PubMed: 30566270]
13. Neuwelt EA, et al., Ultrasmall superparamagnetic iron oxides (USPIOs): a future alternative magnetic resonance (MR) contrast agent for patients at risk for nephrogenic systemic fibrosis (NSF)? *Kidney Int*, 2009. 75(5): p. 465–74. [PubMed: 18843256]
14. Luhar A, et al., Contrast-enhanced magnetic resonance venography in pediatric patients with chronic kidney disease: initial experience with ferumoxytol. *Pediatr Radiol*, 2016. 46(9): p. 1332–40. [PubMed: 27059620]
15. Nguyen KL, et al., Ferumoxytol-enhanced MR Angiography for Vascular Access Mapping before Transcatheter Aortic Valve Replacement in Patients with Renal Impairment: A Step Toward Patient-specific Care. *Radiology*, 2018. 286(1): p. 326–337. [PubMed: 29040038]
16. Toth GB, et al., Current and potential imaging applications of ferumoxytol for magnetic resonance imaging, in *Kidney International* 2017. p. 47–66. [PubMed: 28434822]
17. Wells SA, et al., Pharmacokinetics of Ferumoxytol in the Abdomen and Pelvis: A Dosing Study with 1.5- and 3.0-T MRI Relaxometry. *Radiology*, 2019: p. 190489.
18. Aime S and Caravan P, Biodistribution of gadolinium-based contrast agents, including gadolinium deposition. *J Magn Reson Imaging*, 2009. 30(6): p. 1259–67. [PubMed: 19938038]
19. Theruvath AJ, et al., Brain iron deposition after Ferumoxytol-enhanced MRI: A study of Porcine Brains. *Nanotheranostics*, 2020. 4(4): p. 195–200. [PubMed: 32637297]
20. Stuber M, et al., Positive contrast visualization of iron oxide-labeled stem cells using inversion-recovery with ON-resonant water suppression (IRON). *Magn Reson Med*, 2007. 58(5): p. 1072–7. [PubMed: 17969120]
21. Gharagouzloo CA, et al., Quantitative vascular neuroimaging of the rat brain using superparamagnetic nanoparticles: New insights on vascular organization and brain function. *Neuroimage*, 2017. 163: p. 24–33. [PubMed: 28889004]
22. Knobloch G, et al., Comparison of gadolinium-enhanced and ferumoxytol-enhanced conventional and UTE-MRA for the depiction of the pulmonary vasculature. *Magn Reson Med*, 2019. 82(5): p. 1660–1670. [PubMed: 31228293]
23. Tustison NJ, et al., N4ITK: improved N3 bias correction. *IEEE Trans Med Imaging*, 2010. 29(6): p. 1310–20. [PubMed: 20378467]
24. Avants B, Tustison N, and Song G, Advanced Normalization Tools (ANTs). *Insight Journal*, 2009. 2(365): p. 1–35.
25. Fedorov A, et al., 3D Slicer as an image computing platform for the Quantitative Imaging Network. *Magn Reson Imaging*, 2012. 30(9): p. 1323–41. [PubMed: 22770690]
26. Sigovan M, et al., USPIO-enhanced MR angiography of arteriovenous fistulas in patients with renal failure. *Radiology*, 2012. 265(2): p. 584–590. [PubMed: 22875796]
27. Li Y, et al., The flatness index of inferior vena cava is useful in predicting hypovolemic shock in severe multiple-injury patients. *J Emerg Med*, 2013. 45(6): p. 872–8. [PubMed: 23937811]

28. Gharagouzloo CA, McMahon PN, and Sridhar S, Quantitative contrast-enhanced MRI with superparamagnetic nanoparticles using ultrashort time-to-echo pulse sequences. *Magn Reson Med*, 2015. 74(2): p. 431–41. [PubMed: 25168606]
29. Bak SH, et al., Appropriate Minimal Dose of Gadobutrol for 3D Time-Resolved MRA of the Supra-Aortic Arteries: Comparison with Conventional Single-Phase High-Resolution 3D Contrast-Enhanced MRA. *AJNR Am J Neuroradiol*, 2017. 38(7): p. 1383–1390. [PubMed: 28473338]
30. Dehkharghani S, et al., Dose Reduction in Contrast-Enhanced Cervical MR Angiography: Field Strength Dependency of Vascular Signal Intensity, Contrast Administration, and Arteriographic Quality. *AJR Am J Roentgenol*, 2015. 204(6): p. W701–6. [PubMed: 26001259]
31. Nael K, et al., Combined low-dose contrast-enhanced MR angiography and perfusion for acute ischemic stroke at 3T: A more efficient stroke protocol. *AJNR Am J Neuroradiol*, 2014. 35(6): p. 1078–84. [PubMed: 24503557]
32. Hansmann J, et al., Enhancement characteristics and impact on image quality of two gadolinium chelates at equimolar doses for time-resolved 3-Tesla MR-angiography of the calf station. *PLoS One*, 2014. 9(6): p. e99079. [PubMed: 24893292]
33. Kramer JH, et al., Dynamic and static magnetic resonance angiography of the supra-aortic vessels at 3.0 T: intraindividual comparison of gadobutrol, gadobenate dimeglumine, and gadoterate meglumine at equimolar dose. *Invest Radiol*, 2013. 48(3): p. 121–8. [PubMed: 23211552]
34. Haneder S, et al., Comparison of 0.5 M gadoterate and 1.0 M gadobutrol in peripheral MRA: a prospective, single-center, randomized, crossover, double-blind study. *J Magn Reson Imaging*, 2012. 36(5): p. 1213–21. [PubMed: 22848033]
35. Raman FS, et al., 3.0-T whole-heart coronary magnetic resonance angiography: comparison of gadobenate dimeglumine and gadofosveset trisodium. *Int J Cardiovasc Imaging*, 2013. 29(5): p. 1085–94. [PubMed: 23515949]
36. Schabel MC and Parker DL, Uncertainty and bias in contrast concentration measurements using spoiled gradient echo pulse sequences. *Phys Med Biol*, 2008. 53(9): p. 2345–73. [PubMed: 18421121]
37. Nayak AB, et al., High-resolution, whole-body vascular imaging with ferumoxytol as an alternative to gadolinium agents in a pediatric chronic kidney disease cohort. *Pediatr Nephrol*, 2015. 30(3): p. 515–21. [PubMed: 25212105]
38. Schubert T, et al., Crossover comparison of ferumoxytol and gadobenate dimeglumine for abdominal MR-angiography at 3.0 tesla: Effects of contrast bolus length and flip angle. *J Magn Reson Imaging*, 2017. 45(6): p. 1617–1626. [PubMed: 27862577]
39. Gameraddin M, Normal abdominal aorta diameter on abdominal sonography in healthy asymptomatic adults: impact of age and gender. *Journal of Radiation Research and Applied Sciences*, 2019. 12(1): p. 186–191.
40. François CJ, et al., Renal Arteries: Isotropic, High-Spatial-Resolution, Unenhanced MR Angiography with Three-dimensional Radial Phase Contrast. *Radiology*, 2011. 258(1): p. 254–260. [PubMed: 20980449]
41. Fabrega-Foster KE, et al., Efficacy and safety of gadobutrol-enhanced MRA of the renal arteries: Results from GRAMS (Gadobutrol-enhanced renal artery MRA study), a prospective, intraindividual multicenter phase 3 blinded study. *J Magn Reson Imaging*, 2018. 47(2): p. 572–581. [PubMed: 28574637]
42. Liang KW, et al., The Performance of Noncontrast Magnetic Resonance Angiography in Detecting Renal Artery Stenosis as Compared With Contrast Enhanced Magnetic Resonance Angiography Using Conventional Angiography as a Reference. *J Comput Assist Tomogr*, 2017. 41(4): p. 619–627. [PubMed: 28099225]
43. Bello-Reuss E, Holubec K, and Rajaraman S, Angiogenesis in autosomal-dominant polycystic kidney disease. *Kidney Int*, 2001. 60(1): p. 37–45. [PubMed: 11422734]
44. Ruangwattanapaisarn N, Hsiao A, and Vasanaawala SS, Ferumoxytol as an off-label contrast agent in body 3T MR angiography: a pilot study in children. *Pediatr Radiol*, 2015. 45(6): p. 831–9. [PubMed: 25427433]
45. Aja-Fernandez S, Vegas-Sanchez-Ferrero G, and Tristan-Vega A, Noise estimation in parallel MRI: GRAPPA and SENSE. *Magn Reson Imaging*, 2014. 32(3): p. 281–90. [PubMed: 24418329]

46. Gong IH, et al., Relationship among total kidney volume, renal function and age. *J Urol*, 2012. 187(1): p. 344–9. [PubMed: 22099987]

Author Manuscript

Author Manuscript

Author Manuscript

Author Manuscript



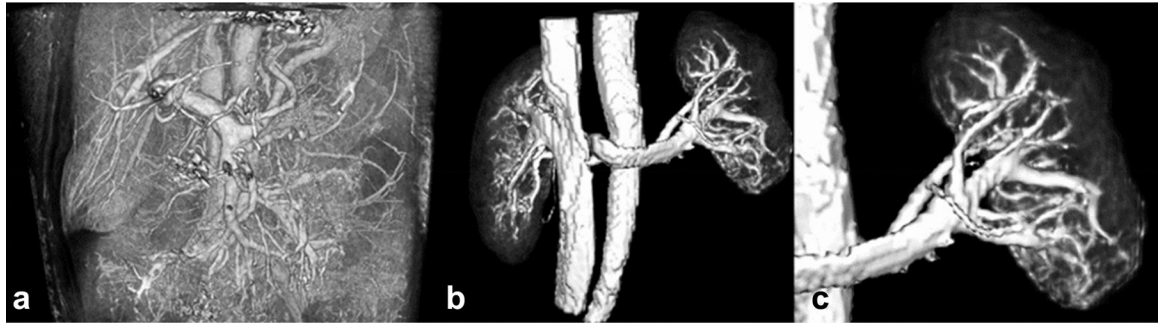


**Figure 1.**

3D renderings of the raw signal intensity of the post-contrast QUTE-CE free-breathing scan capturing **a)** vasculature of the abdominal cavity showing all vessels at the resolution of the scan, **b)** both kidneys and **c)** the left kidney and associated vasculature cropped from the abdominal image in (a).

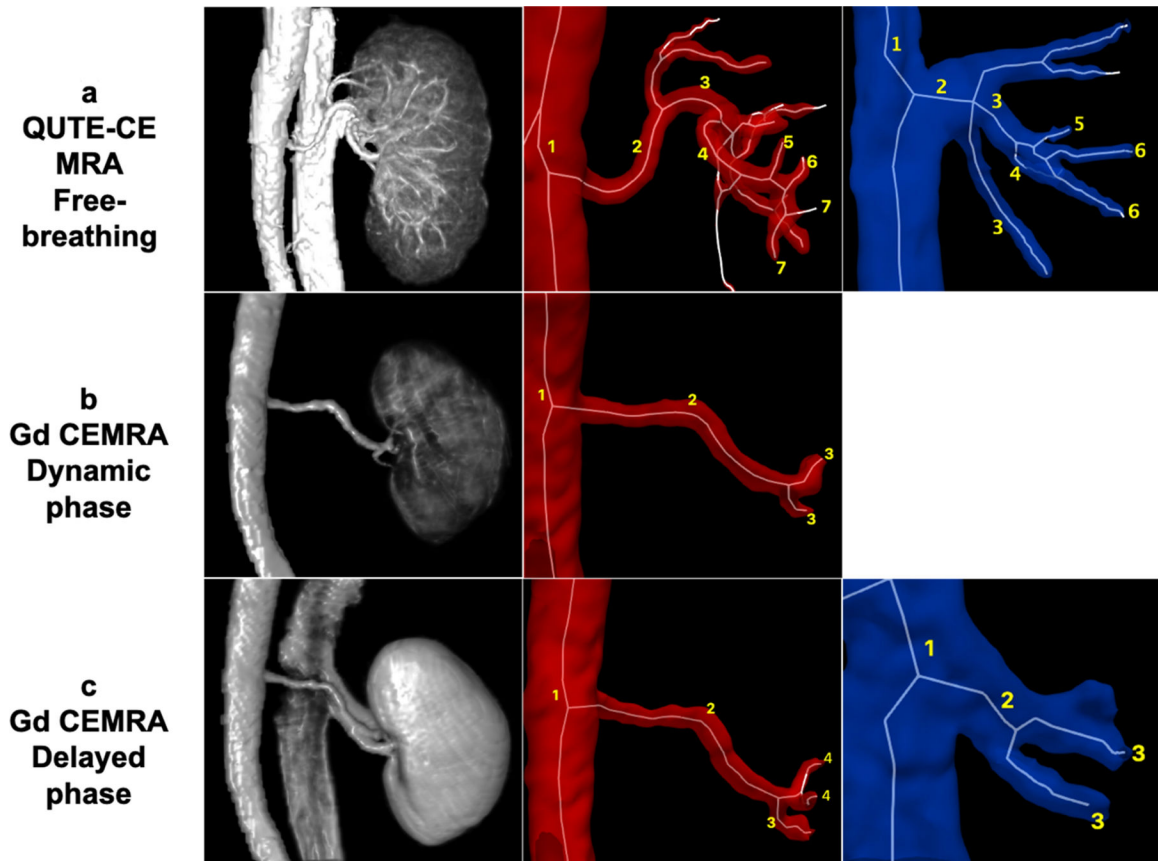


**Figure 2.** Comparison of vessel enhancement for the right kidney between free-breathing QUTE-CE MRA technique and Gd CEMRA. The three columns from left to right are (left) 3D renderings of the post-contrast intensity data, with labeled branching order of the (middle) renal arteries and branching order of the (right) renal veins. **a)** QUTE-CE MRA displays arteries up to the 7th order, veins to the 6th order. **b)** Gd CEMRA: In the dynamic phase image, only the arteries are visible, up to the 3rd branching order. **c)** Gd CEMRA: In the delayed phase image, arteries (to the 4th order) and veins (to the 3rd order) are visible, but vessels inside the kidney are not captured.

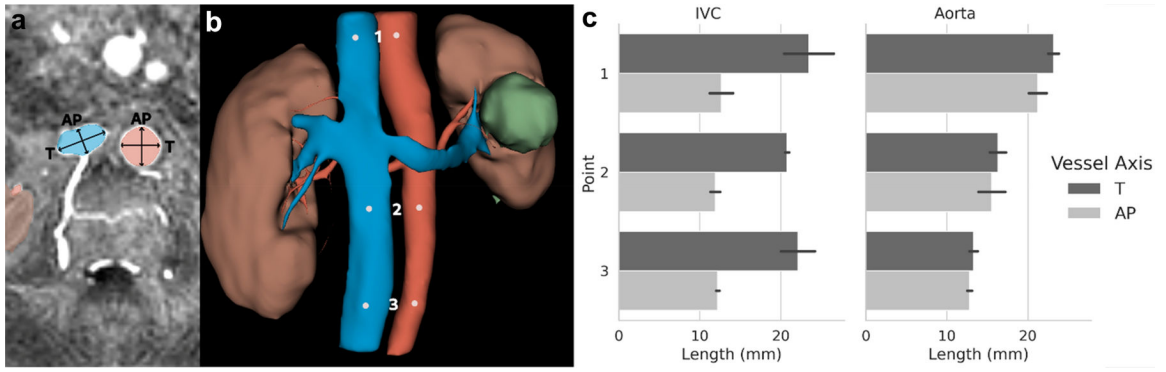


**Figure 3.**  
**a)** Axial cross section of the IVC and abdominal aorta. Segmentations are shaded in blue (vein) and red (artery). The transverse (T) and anteroposterior (AP) diameters used for measurement are indicated by arrows. **b)** 3D rendering of the vessel, kidney and cyst segmentation. Points used for T and AP diameter measurement along the IVC and abdominal aorta are indicated by white points. **c)** Length measurements for the T and AP diameter at each point in the IVC and abdominal aorta.

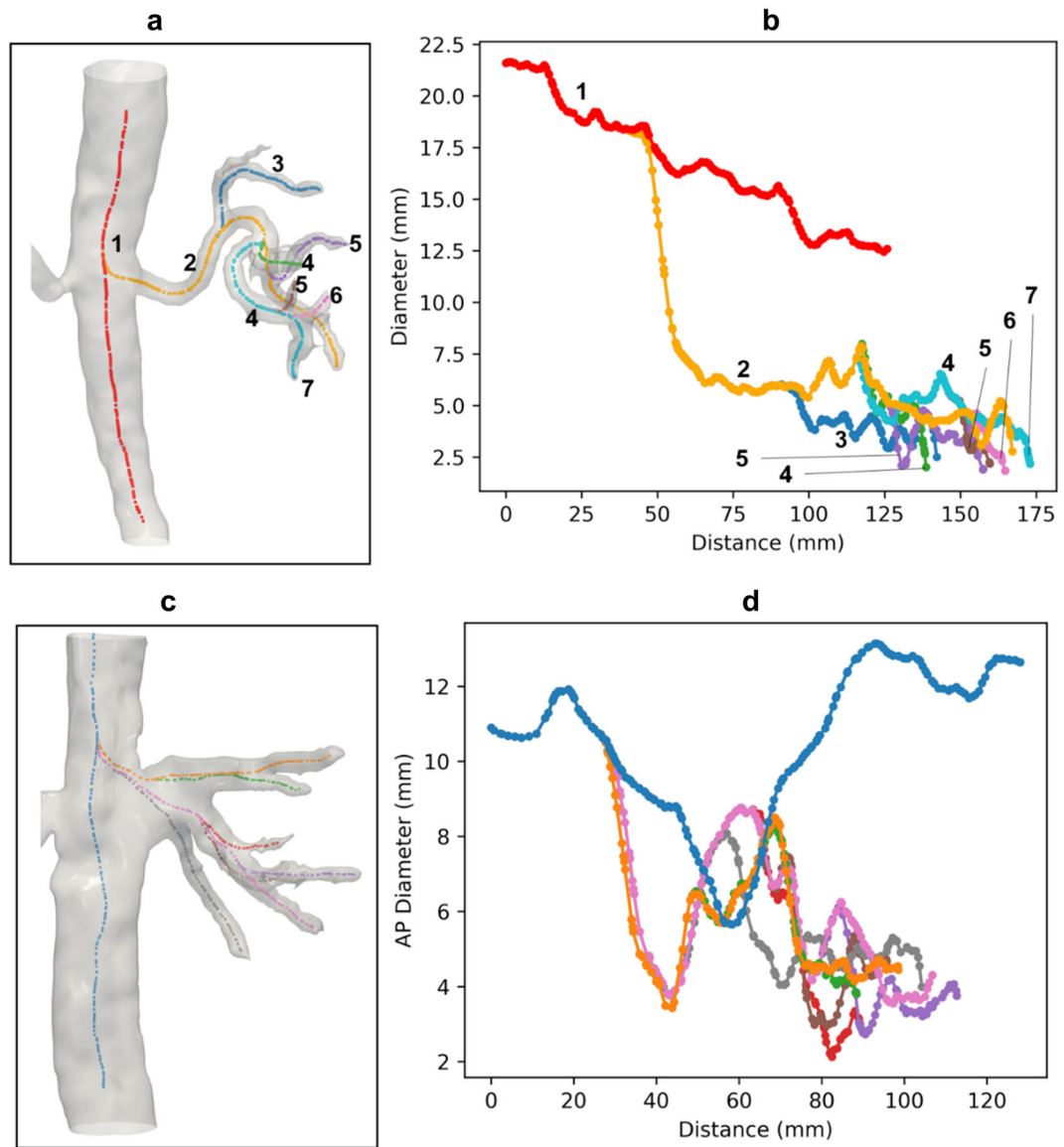


**Figure 4.**

**a)** Surface model and generated centerlines of the aorta and arteries in the right kidney of the same subject shown in Figure 2. **b)** Diameter plot with color coded and branching order labeled corresponding to the vessels shown in (a). **c)** Surface model and generated centerlines of the inferior vena cava and veins in the right kidney of the same subject. **d)** Anteroposterior (AP) diameter with color coded corresponding to the vessels shown in (c). Note that y-axis in the plot is the AP diameter due to the algorithm used in the automatic measurement (maximum inscribed spheres).

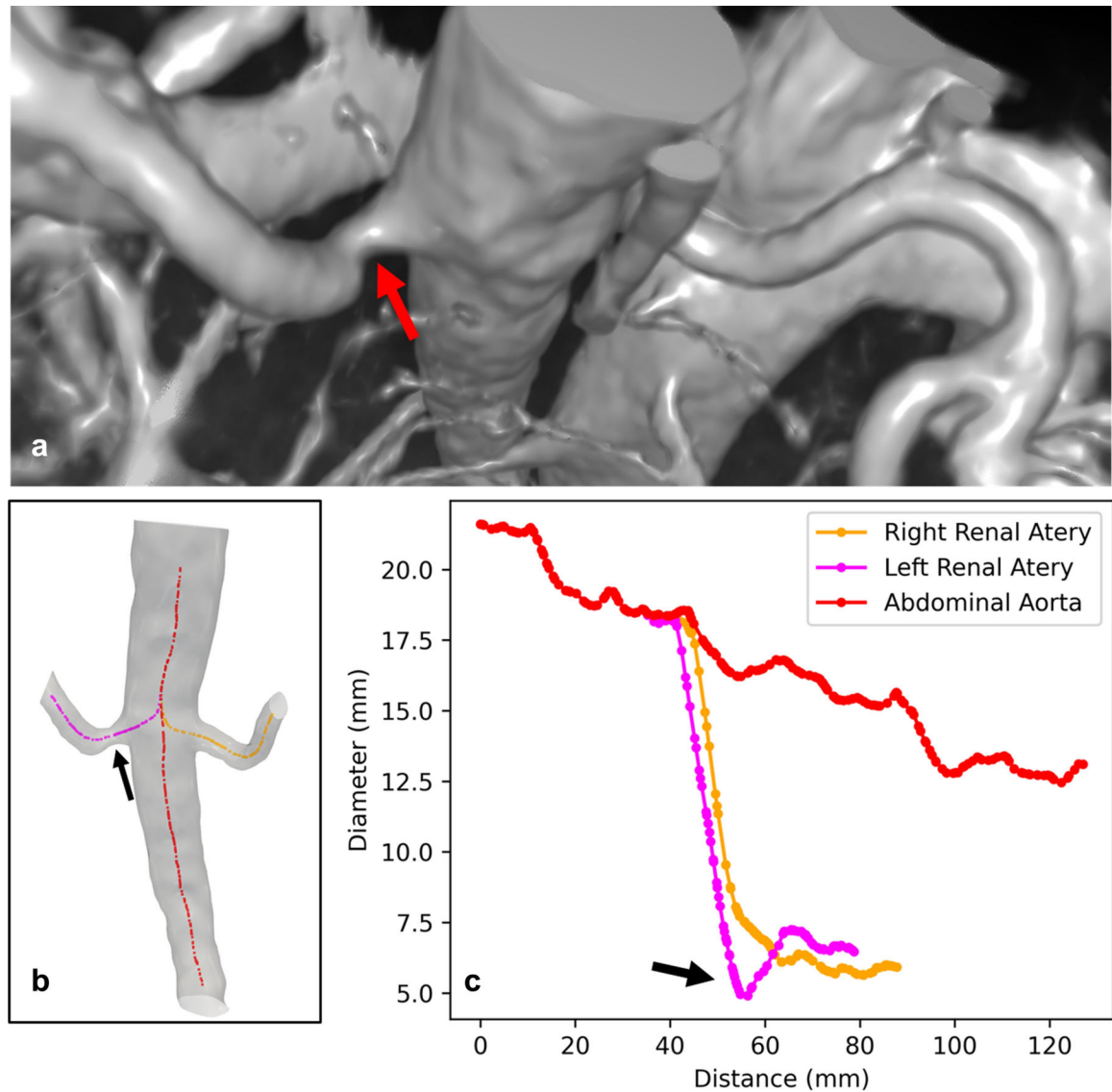


**Figure 5.** Narrowing of left renal artery is demonstrated in **a)** 3D rendering of the raw post-contrast QUTE-CE free-breathing intensity data, **b)** surface model of the aorta and renal arteries and generated centerlines, **c)** diameter plot at centerline points along the vessels. The reduction in left renal artery diameter is over 28.7% but no narrowing shown in right renal artery.

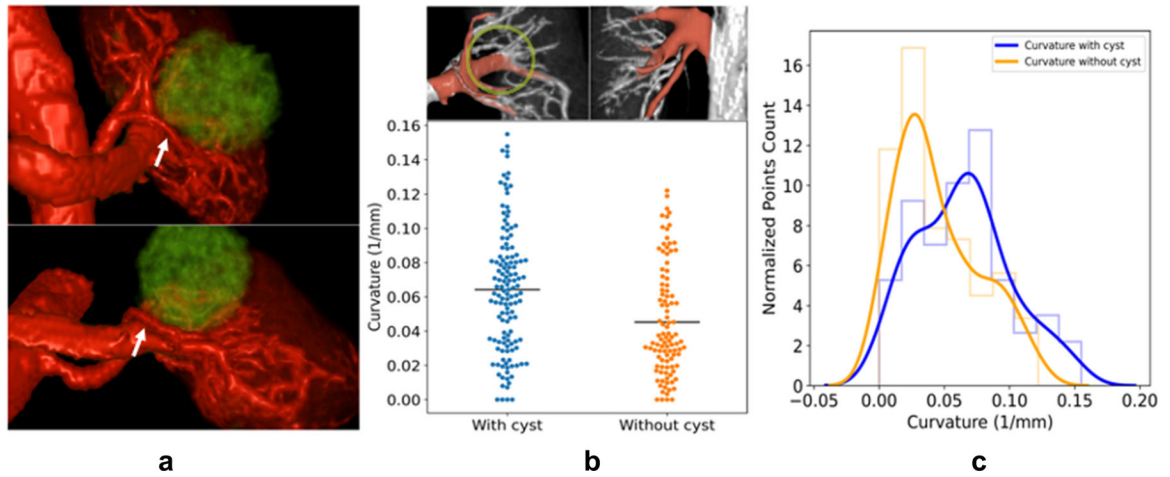


**Figure 6.**

**a)** 3D renderings from coronal and axial view of the same kidney and vasculature shown in Fig. 1, rendered with vessels in red and cysts in green, white arrow points out vessels displaced around the cyst. **b) Top:** Vessels encircling the cyst were used for analysis and are colored in red. These vessels are reorganized around the cyst. The approximate border of the cyst is indicated with a light green circle. In the other non-cyst kidney of the same subject, corresponding vessels with the same branching order are colored in red. **Bottom:** Curvature is compared between centerline points in vessels with and without cyst, respectively. Vessels around the cyst have higher curvature than those without cyst ( $0.06 \pm 0.04$  vs  $0.05 \pm 0.03$ ,  $P < 0.001$ ). Black line indicates the mean of each group. **c)** Normalized histogram of the vascular curvature and the estimated probability density function. The curvature distribution for vessels around the cyst is shifted to the right and the peak appears at higher curvature value.



**Table 1.**

Sequence parameters and quantitative angiographic metrics measured on IVC and abdominal aorta

	Technique	QUTE-CE		QUTE-CE	Gd CEMRA		
	Scan Type	Breath-hold		Free-breathing	Breath-hold		
		a	b		dynamic	delayed 1	delayed 2
<b>Parameters</b>	TE (ms)	0.05	0.05	0.05	1.03	1.03	1.03
	TR (ms)	2.42	2.42	2.91 – 3.10	3.02	3.02	3.02
	FA (deg)	13*	5	13.5	20	20	20
	Acquired Resolution (mm <sup>2</sup> )	2.14 × 2.14	2.08 × 2.08	1.56 × 1.56	1.25 × 1.78	1.25 × 1.78	1.25 × 1.78
	Slice Thickness (mm)	2.5	2.5	1.56 – 1.76	2.5	2.5	2.5
	Voxel Size (mm <sup>3</sup> )	11.48	10.85	4.05 ± 0.35	5.56	5.56	5.56
	Acquisition Time (mm:ss)	00:16	00:16	~12:00	00:52	00:34	00:56
<b>Artery</b>	SNR	1751 ± 248	3209 ± 1395	182 ± 64	238	216	134
	CNR	1030 ± 42	1222 ± 607	111 ± 29	195	164	97
	ISH	0.034 ± 0.006	0.049 ± 0.009	0.068 ± 0.022	0.266	0.111	0.228
<b>Vein</b>	SNR	1797 ± 126	3355 ± 1575	181 ± 70	13	85	106
	CNR	1076 ± 161	1368 ± 786	111 ± 35	-30	35	69
	ISH	0.031 ± 0.004	0.039 ± 0.017	0.058 ± 0.011	0.289	0.132	0.081

Note: SNR = Signal-to-Noise Ratio, CNR = Contrast-to-Noise Ratio, ISH = Intraluminal Signal Heterogeneity, QUTE-CE = Quantitative Ultrashort-Time-to-Echo Contrast Enhanced, Gd = Gadolinium, CEMRA = Contrast Enhanced Magnetic Resonance Angiography.

\* FA reduced to 11 degrees in one subject.

**Table 2.**

Subject data and kidney metrics

Subject	Sex	Age	CKD stage	Side	Kidney Vol. (ml)	Cyst Vol. (ml)	Cysts/Kidney Ratio	Renal Artery Diameter (measurement $\pm$ error) (mm)	Degree of Narrowing
1	F	62	N/A	Right	204.9	0.2	0.1%	6.4 $\pm$ 0.7	16.2%
				Left	129.0	17.1	13.3%	4.6 $\pm$ 0.7	34.9%
2	F	48	N/A	Right	233.9	N/A	N/A	6.8 $\pm$ 0.6	13.2%
				Left	201.0	N/A	N/A	7.5 $\pm$ 0.8	22.5%
3	F	70	N/A	Right	215.1	0.3	0.1%	6.0 $\pm$ 0.2	5.4%
				Left	158.2	32.2	20.2%	6.8 $\pm$ 0.3	28.7%
4	M	76	5, eGFR = 10 mL/min/1.73m <sup>2</sup>	Right	110.3	3.7	3.4%	4.5 $\pm$ 0.3	13.1%
				Left	114.3	24.3	21.3%	4.7 $\pm$ 0.4	10.9%
Mean		64			170.8	13.0	9.7%	5.9	18.1%
STD		12			49.0	13.6	9.8%	1.2	9.9%

Note: CKD = Chronic Kidney Disease, eGFR = estimated Glomerular Filtration Rate, STD = Standard Deviation.